



# Non-associated and Non-quadratic Characteristics in Plastic Anisotropy of Automotive Lightweight Sheet Metals

Yong Hou<sup>1</sup> · Junying Min<sup>2</sup> · Myoung-Gyu Lee<sup>1</sup>

Received: 13 January 2023 / Accepted: 4 May 2023 / Published online: 8 September 2023  
© The Author(s) 2023

## Abstract

Lightweight sheet metals are highly desirable for automotive applications due to their exceptional strength-to-density ratio. An accurate description of the pronounced plastic anisotropy exhibited by these materials in finite element analysis requires advanced plasticity models. In recent years, significant efforts have been devoted to developing plasticity models and numerical analysis methods based on the non-associated flow rule (non-AFR). In this work, a newly proposed coupled quadratic and non-quadratic model under non-AFR is utilized to comprehensively investigate the non-associated and non-quadratic characteristics during the yielding of three lightweight sheet metals, i.e., dual-phase steel DP980, TRIP-assisted steel QP980, and aluminum alloy AA5754-O. These materials are subjected to various proportional loading paths, including uniaxial tensile tests with a 15° increment, uniaxial compressive tests with a 45° increment, in-plane torsion tests, and biaxial tensile tests using laser-deposited arm-strengthened cruciform specimens. Results show that the non-AFR approach provides an effective means for accurately modeling the yield behavior, including yield stresses and the direction of plastic strain rates, simultaneously, utilizing two separate functions and a simple calibration procedure. The introduction of the non-quadratic plastic potential reduces the average errors in angle when predicting plastic strain directions by the quadratic plastic potential function. Specifically, for DP980, the average error is reduced from 3.1° to 0.9°, for QP980 it is reduced from 6.1° to 3.9°, and for AA5754-O it is reduced from 7.0° to 0.2°. This highlights the importance of considering the non-quadratic characteristic in plasticity modeling, especially for aluminum alloys such as AA5754-O.

**Keywords** Yield behavior · Non-associated flow rule · Non-quadratic · Lightweight sheet metal

## Abbreviations

AA	Aluminium alloy	Non-AFR	Non-associated flow rule
AFR	Associated flow rule	PS	Plane strain
BCC	Body-centered cubic	PSY2019	Park-Stoughton-Yoon 2019 yield function
CQI	Coupled quadratic and stress-invariant-based	Q&P	Quenching and partitioning
CQN	Coupled quadratic and non-quadratic	RA	Retained austenite
DD	Diagonal direction	RD	Rolling direction
DP	Dual-phase	SD	Strength differential
FCC	Face-centered cubic	TD	Transverse direction, 90° to the RD
GTN	Gurson-Tvergaard-Needleman	TRIP	Transformation induced plasticity
MSR	Mean square root	UC	Uniaxial compression
ND	Normal direction	UT	Uniaxial tension
		WEDM	Wire electrical discharge machining

✉ Myoung-Gyu Lee  
myounglee@snu.ac.kr

<sup>1</sup> Department of Materials Science and Engineering and RIAM, Seoul National University, Seoul 08826, South Korea

<sup>2</sup> School of Mechanical Engineering, Tongji University, Shanghai 201804, China

## 1 Introduction

With the rapid advancement of fuel economy, the demand for weight reduction in the automobile industry has significantly increased. To meet this demand, conventional materials are being replaced by stronger and lighter sheet materials, such as

advanced high-strength steels and aluminum alloys. To reduce manufacturing costs, the optimization of automobile manufacturing processes through finite element analysis is considered an effective approach. One crucial aspect of simulating metal forming processes is the application of accurate constitutive models.

Planar anisotropic characteristics in lightweight sheet metals are typically characterized by their strength, specifically the yield stress, as well as their plastic flow, represented by the r-value in given orientations. To capture this plastic anisotropy resulting from the rolling process, various anisotropic yield criteria have been proposed. Hill [1] proposed a classical quadratic yield function, which applies the r-values to describe the deformation anisotropy. Barlat and Lian [2] extended the isotropic Hosford1972 yield criterion [3] to account for in-plane anisotropy. Gotoh [4] proposed the first fourth-order polynomial yield criterion, while other researchers have developed different polynomial yield surfaces [5–7]. Another classical approach involves the linear transformation of the Cauchy stress tensor, which enables the extension of isotropic yield functions to include anisotropy [8–11]. The Yld2k-2d model with eight parameters [8] has been developed to capture yield stresses and r-values by a linear combination of two functions. Cazacu and Barlat [12] proposed a representative theoretical framework for the second and third stress invariants. Building upon the linear transformation or the representative theoretical framework, several advanced anisotropic yield criteria have been developed [13–16].

Foregoing anisotropic yield functions have generally been developed based on the associated flow rule (AFR), where the yield stress function is assumed to be identical to the plastic potential function. Nevertheless, it has always been a challenge to capture the fully anisotropic features, including yield stress and r-value, using a single function. This has led scholars to question the validity of AFR in plasticity theories. Spitzig and Richmond [17] experimentally observed that the small pressure dependence of yielding in steels and aluminum was not accompanied by an expected plastic dilatation from the AFR assumption. Stoughton [18] proposed a quadratic non-AFR model (Stoughton2002), which showed remarkable agreement with data from uniaxial tension and equi-biaxial tension tests. So far, the existing plasticity models can be divided into two categories, as shown in Fig. 1, where  $\bar{\sigma}_y$  and  $\bar{\sigma}_p$  are the yield stress and plastic potential functions, respectively.  $\sigma_{11}$  and  $\sigma_{22}$  are two normal stress components.  $d\epsilon^p$  is the direction of plastic flow,  $d\lambda$  is the rate of plastic compliance factor, and  $\sigma$  is the Cauchy stress tensor. One category of plasticity model is based upon the framework of the AFR. The other type is the plasticity model under the non-associated flow rule (non-AFR), where the yield stress function and the plastic potential function are two independent functions used to describe the yield stresses and the flow direction, respectively. A comprehensive review of recent advances in yield

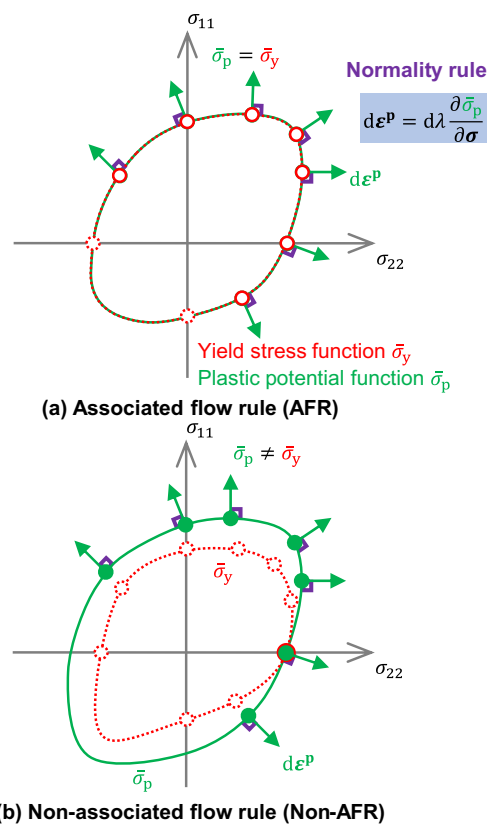


Fig. 1 Plasticity models under **a** associated flow rule (AFR), and **b** non-AFR

criteria, flow rules, and hardening law can be found in the work of Hou et al. [19].

Over the past decade, researchers generally believe that non-AFR provides a simple and efficient approach for modeling the anisotropic yielding and plastic flow of metallic materials. Plasticity models under non-AFR were widely developed [20–26].

Stoughton and Yoon [20] extended the yield stress function in the non-AFR Stoughton2002 model to include pressure sensitivity. Min et al. [21] developed a novel non-AFR non-quadratic plastic potential function on the basis of the Barlat-Lian89 yield function [2]. Lee et al. [22] proposed the CQN (coupling of quadratic and non-quadratic functions) yield stress function under non-AFR. Later, Hou et al. [27] developed the CQN model by introducing the pressure sensitivity to the quadratic Hill48 function and applied the modified CQN to capture the evolving strength differential (SD) effect. Park et al. [23] proposed a non-AFR criterion for the general description of anisotropic hardening with the SD effect based on the scaling and asymmetry terms.

In addition, the flexibility of the anisotropic Drucker function was improved by Lou and Yoon [28] by constructing a plasticity model under non-AFR. Chen et al. [29] presented a non-AFR pressure-insensitive function to describe the

evolution of yield surface and adjust the curvature of yield loci in plane strain tension. Hou et al. [30] proposed a simple coupling of asymmetric quadratic and isotropic stress-invariant-based yield functions (CQI) under non-AFR to simultaneously model stress anisotropy, SD effect, and anisotropic hardening. Hu et al. [31] developed an asymmetric yield function by introducing asymmetrical parameters into the Yld2k-2d function. To capture plastic anisotropy under plane strain conditions, fourth-order polynomial functions of the stress tensor were applied to the yield stress and plastic potential functions under non-AFR by Hou et al. [25]. Most recently, Lou et al. [26] proposed a general stress-invariant-based yield function under non-AFR to capture differential yield stresses under four stress states.

There have been many studies on the application of non-AFR plasticity models. Safaei et al. [32] presented a comparative analysis of the computational efficiency and accuracy of four stress integration algorithms for elastic–plastic constitutive models under non-AFR and AFR. Du et al. [33] found that a non-AFR plasticity model composed of the PSY2019 yield stress function [23] and Hou et al. 2020 plastic potential function [34] more accurately characterizes the asymmetric anisotropic yield and flow of 6016-T4 aluminum alloy and DP490 steel than other investigated asymmetric yield criteria. Mu et al. [35] accurately captured the anisotropic hardening and evolution of  $r$ -values in DC06 steel sheets under proportional loading using an evolving non-AFR Hill48 model. Bandyopadhyay et al. [36] found that finite element simulation implementing the non-AFR plasticity model (Hill48) predicted the deep drawing behaviour of tailor-welded blanks made from dual-phase steel (DP980) more accurately compared with that under AFR.

As an effective method to model yield surface and  $r$ -values, the non-AFR plasticity model was proved to easily consider kinematic, distortional hardening characteristics. Lee et al. [37] proposed a scheme to combine a kinematic hardening model with a condition function to accurately capture both asymmetric plastic behavior under cycling loading and anisotropic hardening under monotonic loading. Later, both Bauschinger effect and anisotropic hardening behavior were captured simultaneously by Lee et al. [38] via an extended model of the CQN yield stress function with the homogeneous anisotropic hardening (HAH) model [39]. Hou et al. [40] developed a non-AFR plasticity model based on the distortional hardening concept and the CQI yield function. Hu and Yoon [41] proposed an anisotropic distortional hardening model under non-AFR by evolving the distortional yield criterion.

The non-AFR plasticity model can be easily joined with the Marciniak–Kuczynski theory and ductile fracture criteria to predict the formability of sheet metals. Shen et al.

[42] coupled the Marciniak–Kuczynski localization criterion with the evolving non-AFR Hill48 plasticity model. Vobejda et al. [43] stated that the non-AFR plasticity model provided an alternative solution to the problems in the description of stress state and deformation when predicting ductile fracture of 2024-T351 aluminum alloy. Wu et al. [44] introduced the Yld91 yield stress under AFR and non-AFR into the extended isotropic Gurson-Tvergaard-Needleman (GTN) model to predict the anisotropic fracture initiation of 2024-T351 aluminum alloy under in-plane tension and shear.

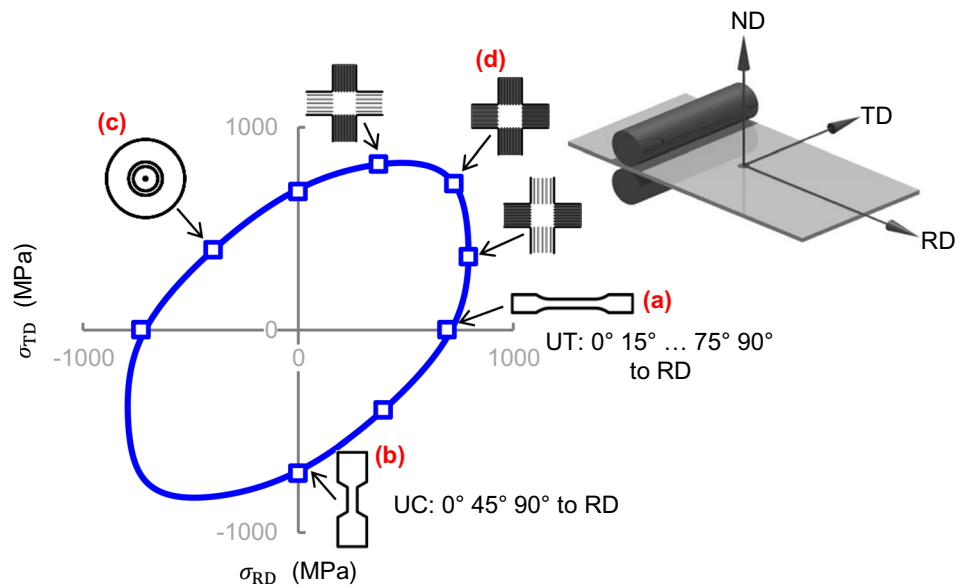
Due to the challenge in mechanical testing of sheet metals, e.g. measurements of stress vs. strain curves and strain rate ratios of sheet metals subjected to large plastic strains under plane strain tension, most of the non-AFR models do not consider the non-quadratic characteristics in the yield surface or plastic potential surface of sheet metals, or simply determine one number for the exponent of yield functions, e.g. 6 and 8 for metals with body-centered cubic (BCC) and face-centered cubic (FCC) crystal systems, respectively.

Based on the above literature review, it can be concluded that the quantitative evaluation of non-associated and non-quadratic features in the yielding behavior of lightweight sheet metals is poorly studied in the literature. In this work, based on the advanced mechanical characterization, a systematic investigation was performed on the yield behavior of three different types of sheet metals including one dual-phase steel, one TRIP-assisted steel, and one aluminum alloy. The focus was put on the non-associated and non-quadratic characteristics in yielding at one given plastic strain level of sheet metals. A non-AFR model was employed to describe the yield surface of sheet metals, and based on the proposed parameter identification approach, the non-quadratic was detailed investigated. This work is divided into the following chapters. The investigated materials and mechanical characterization including various proportional loading paths are provided in Sect. 2. The proposed plasticity model under non-AFR is clarified in Sect. 3. The results and discussion based on the experimental investigation and constitutive modeling are presented in Sect. 4. Finally, Sect. 5 summarizes the main conclusions.

## 2 Materials and Mechanical Characterization

This study examines commercially available materials, including 1.2 mm thick dual-phase steel (DP980) with a grade of 980 MPa, 1.0 mm thick quenching-partitioning steel (QP980) with a grade of 980 MPa, and 2.0 mm thick aluminum alloy (AA5754-O). Note that QP980 is a third-generation advanced high-strength steel with a microstructure consisting of ferrite, martensite, and approximately 12.6 vol.% metastable retained

**Fig. 2** Mechanical tests to characterize yield loci of automotive lightweight sheet metals: **a** uniaxial tension, **b** uniaxial compression, **c** in-plane torsion, and **d** biaxial tension with laser-deposited cruciform specimens



austenite (RA). The deformation-induced martensite transformation is the underlying mechanism of good formability of QP980 steel, well known as the TRIP effect.

As shown in Fig. 2, proportional loading paths are achieved using a series of mechanical tests including (a) uniaxial tension, (b) uniaxial compression, (c) in-plane torsion, and (d) biaxial tension with laser-deposited cruciform specimens at room temperature and quasi-static strain rates. The blue hollow points in Fig. 2 represent the measured initial yielding stress pairs ( $\sigma_{RD}$ ,  $\sigma_{TD}$ ) in the normal plane of sheet metal under various stress states, meaning that the material reaches its yield limit and becomes plastic. The dotted lines represent the proportional loading paths from the as-received state (zero stress) of the sheet metals. The sheet metals are fabricated by the rolling process as shown in the top right-hand corner of Fig. 2, where RD, TD, and ND stand for the rolling, transverse, and normal directions, respectively.

## 2.1 Uniaxial Tension

Dog-bone specimens according to ASTM E8 Standard are cut by wire electrical discharge machining (WEDM) at 15° increments from 0° to 90° to the rolling direction (RD). The gauge area is 50 mm by 12.5 mm. Uniaxial tensile tests with a crosshead speed of ~10 mm/min are performed on a universal testing machine (UTM) MTS E45.105 (see Fig. 3) to obtain stress vs. strain curves and r-values under uniaxial tension conditions at quasi-static strain rates.

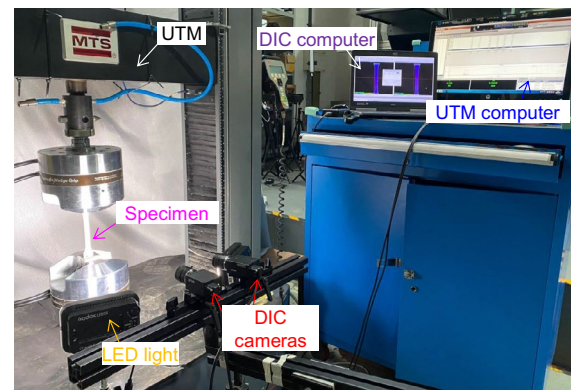
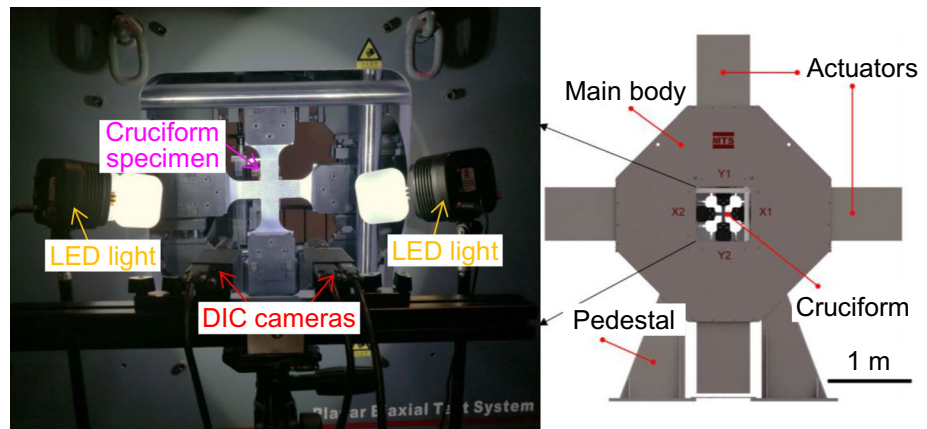


**Fig. 3** A universal testing machine MTS E45.105 with the digital image correlation system to measure the strain fields of specimens

## 2.2 Uniaxial Compression

Uniaxial compression tests are performed on the universal testing machine MTS E45.105 (Fig. 3) with the aid of a supporting fixture, which was designed to suppress the premature buckling of the thin sheet specimens in the thickness direction during the axial compression [45]. The specialized specimens, which are cut by WEDM along 0°, 45°, and 90° to the RD, have a rectangular gauge area of 36.2 mm by 15.2 mm. A constant crosshead speed of 2 mm/min was used in the uniaxial compression tests. A nominal side force of ~3.0 kN is applied between the sample and the supporting fixture. 0.1-mm-thick Teflon sheets are attached between the sample and the supporting fixture with lubricating grease in order to minimize friction.

**Fig. 4** The biaxial testing system MTS BIA5105 with the digital image correlation system



### 2.3 In-plane Torsion

The in-plane torsion test introduced by Tekkaya et al. [46] was performed on a torsion device to measure stress vs. strain curves under simple shear conditions. The radii of the inner and outer clamps were 15 mm and 30 mm, respectively. The inner clamps were fixed and loaded on a Zwick universal testing machine, while the outer clamps were rotated. Hence, the annular free area of a circular specimen between the inner and outer clamps was deformed under simple shear. During in-plane torsion testing, the rotation angle of the outer clamps was measured with a rotation angle sensor with an accuracy of  $0.018^\circ$ , and the applied torque was measured with a sensor. Shear strain and shear stress decrease with the increasing radial distance from the center of the circular specimen.

### 2.4 Biaxial Tension with Cruciform Specimens

In order to measure the yield loci and the plastic strain rate in the biaxial tension condition, the biaxial tension tests with the cruciform specimens are used in this work. The geometries of cruciform specimens are based on the ISO standard [47], and the arms of cruciform are strengthened using a laser deposition process [48, 49]. The gauge region is 45 mm by 45 mm square, which is located in the middle of the cruciform and enclosed by four slit arms with laser deposition. The cruciform specimens are cut by laser along the RD-TD direction of sheet metals. Biaxial tensile tests are performed on a biaxial testing system MTS BIA5105, as shown in Fig. 4. Three fixed ratios of biaxial forces, 1:2, 1:1, and 2:1 are adopted to test the cruciform specimens and investigate the yield behavior and plastic flow along various stress paths in the first quadrant of stress space.

At least three tests are performed for each condition to guarantee the repeatability of the measurements. Digital image correlation techniques are applied to monitor the evolution of strain fields of specimens in all mechanical tests following procedures described by Jones and Iadicola [50]. Detailed

information on these involved mechanical characterization methods and data post-processing refers to a previous study [51].

## 3 Plasticity Model Under Non-AFR

### 3.1 Yield Stress Function

A non-AFR model was developed to accurately describe the evolving yield behavior of sheet metals [34]. The coupling framework proposed by Lee et al. [22] was used to construct the yield stress function, as shown in Eq. (1)

$$f_{\text{Coup}}(\boldsymbol{\sigma}, \bar{\lambda}) = \left[ f_{\text{Quad}}(\boldsymbol{\sigma}, \bar{\lambda}) \cdot f_{\text{Non-Q}}(\boldsymbol{\sigma})^{m-1} \right]^{\frac{1}{m}} = 1 \quad (1)$$

where  $f_{\text{Coup}}(\boldsymbol{\sigma}, \bar{\lambda})$  is the proposed yield function, and  $f_{\text{Quad}}(\boldsymbol{\sigma}, \bar{\lambda})$  is the quadratic part, which plays a role to describe the plastic anisotropy.  $f_{\text{Non-Q}}(\boldsymbol{\sigma})$  is an isotropic non-quadratic part to control the curvature of the yield surface.  $\boldsymbol{\sigma}$  is the stress tensor, and  $\bar{\lambda}$  represents the plastic compliance factor, and  $m$  is the exponent constant of the yield function. The material goes through elastic deformation when  $f_{\text{Coup}}(\boldsymbol{\sigma}, \bar{\lambda}) < 1$ , but the elastic-plastic deformation when  $f_{\text{Coup}}(\boldsymbol{\sigma}, \bar{\lambda}) = 1$ .

The Spitzig and Richmond formula [17] is added to the quadratic Hill48 function under plane stress conditions, as shown in Eq. (2), to capture the SD effect along the RD, DD, and TD of sheet metal.

$$f_{\text{Quad}}(\boldsymbol{\sigma}, \bar{\lambda}) = a_y \sigma_{11} + b_y \sigma_{22} + c_y \sigma_{12} + \sqrt{d_y \sigma_{11}^2 + e_y \sigma_{22}^2 - f_y \sigma_{11} \sigma_{22} + g_y \sigma_{12}^2} \quad (2)$$

where  $\sigma_{11}$  and  $\sigma_{22}$  are normal stress components, and  $\sigma_{12}$  is a shear stress component.  $a_y \sim g_y$  are the model parameters.  $a_y$ ,  $b_y$ , and  $c_y$  are related to the SD effect along the RD, TD, and

DD of sheet metals. In general,  $a_y$ ,  $b_y$ , and  $c_y$  will be found to be small and may be set to zero when the SD effect can be ignored.  $d_y$ ,  $e_y$ ,  $f_y$ , and  $g_y$  are related to the plastic anisotropy of sheet metals. The anisotropic parameters can be identified explicitly according to Eq. (3).

$$a_y = \frac{1}{2} \left( \frac{1}{\sigma_{T0}^m(\bar{\lambda})} - \frac{1}{\sigma_{C0}^m(\bar{\lambda})} \right) \tag{3a}$$

$$b_y = \frac{1}{2} \left( \frac{1}{\sigma_{T90}^m(\bar{\lambda})} - \frac{1}{\sigma_{C90}^m(\bar{\lambda})} \right) \tag{3b}$$

$$c_y = \left( \frac{1}{\sigma_{T45}^m(\bar{\lambda})} - \frac{1}{\sigma_{C45}^m(\bar{\lambda})} \right) - a_y - b_y \tag{3c}$$

$$d_y = \frac{1}{4} \left( \frac{1}{\sigma_{T0}^m(\bar{\lambda})} + \frac{1}{\sigma_{C0}^m(\bar{\lambda})} \right)^2 \tag{3d}$$

$$e_y = \frac{1}{4} \left( \frac{1}{\sigma_{T90}^m(\bar{\lambda})} + \frac{1}{\sigma_{C90}^m(\bar{\lambda})} \right)^2 \tag{3e}$$

$$f_y = d_y + e_y - \left( \frac{1}{\sigma_b^m(\bar{\lambda})} - a_y - b_y \right)^2 \tag{3f}$$

$$g_y = \left( \frac{1}{\sigma_{T45}^m(\bar{\lambda})} + \frac{1}{\sigma_{C45}^m(\bar{\lambda})} \right)^2 - \left( \frac{1}{\sigma_b^m(\bar{\lambda})} - a_y - b_y \right)^2 \tag{3g}$$

where  $\sigma_{T0}(\bar{\lambda})$ ,  $\sigma_{T45}(\bar{\lambda})$  and  $\sigma_{T90}(\bar{\lambda})$  represent uniaxial tensile yield stresses along the RD, DD, and TD, respectively;  $\sigma_{C0}(\bar{\lambda})$ ,  $\sigma_{C45}(\bar{\lambda})$  and  $\sigma_{C90}(\bar{\lambda})$  are uniaxial compressive yield stresses along the RD, DD, and TD, respectively, which are assumed as positive values.  $\sigma_b(\bar{\lambda})$  denotes the yield stress under equi-biaxial tension as a function of the plastic compliance factor  $\bar{\lambda}$ .

An isotropic non-quadratic yield function, as shown in Eq. (4), was coupled with  $f_{Quad}(\sigma, \bar{\lambda})$  to consider the non-quadratic characteristic.

$$f_{Non-Q}(\sigma) = \frac{3}{(2^{n_{HH}} + 2)^{1/n_{HH}} + 3 \cdot 2^{1/n_{HH}}} \cdot [f_{HH}(\sigma) + f_{IHH}(\sigma)] \tag{4a}$$

$$f_{HH}(\sigma) = (|s_1 - s_2|^{n_{HH}} + |s_2 - s_3|^{n_{HH}} + |s_3 - s_1|^{n_{HH}})^{1/n_{HH}} \tag{4b}$$

$$f_{IHH}(\sigma) = (|s_1|^{n_{IHH}} + |s_2|^{n_{IHH}} + |s_3|^{n_{IHH}})^{1/n_{IHH}} \tag{4c}$$

where  $n_{HH}$  and  $n_{IHH}$  are two independent exponent constants.  $s_1$ ,  $s_2$ , and  $s_3$  are the principal values of the stress deviator. The averaged ratio of yield stresses under plane strain and simple shear to yield stress under uniaxial tension based on experimental data was used to determine the exponents  $n_{HH}$  and  $n_{IHH}$  in Eq. (4).

### 3.2 Plastic Potential Function

In the non-AFR model, a plastic potential function, as expressed by Eq. (5), is used to capture the direction of the plastic strain rate under plane stress conditions.

$$\tilde{\sigma}_p(\sigma, \bar{\lambda}) = a_p \sigma_{11} + b_p \sigma_{22} + c_p \sigma_{12} + \tilde{\sigma}'_p(\sigma, \bar{\lambda}) = \sigma_Y(\bar{\lambda}) \tag{5a}$$

$$\tilde{\sigma}'_p(\sigma, \bar{\lambda}) = [d_p(K_1 + K_2)^{k_p} + d_p(K_1 - K_2)^{k_p} + e_p(2K_2)^{k_p}]^{1/k_p} \tag{5b}$$

$$K_1 = \frac{\sigma_{11} + f_p \sigma_{22}}{2} \tag{5c}$$

$$K_2 = \sqrt{\left( \frac{\sigma_{11} - g_p \sigma_{22}}{2} \right)^2 + (2h_p \sigma_{12})^2} \tag{5d}$$

where  $\tilde{\sigma}_p(\sigma, \bar{\lambda})$  is the proposed plastic potential function, and  $\sigma_Y$  is the yield stress under UT along the RD of sheet metals.  $K_1$  and  $K_2$  are two anisotropic principal stresses. The exponent constant  $k_p$  is a positive integer number.  $a_p \sim h_p$  are eight model parameters, which can be determined through an optimization approach to minimize the errors between the experimental data and the values predicted by the plastic potential function.  $a_p$ ,  $b_p$ , and  $c_p$  are related to the asymmetry of plastic potential along the RD, TD, and DD of sheet metals.

## 4 Results and discussion

### 4.1 Experimental Yield Loci

Figure 5 presents the experimental yield loci of DP980, QP980, and AA5754-O associated with the increasing plastic compliance factor  $\bar{\lambda}$ . These yield loci are acquired

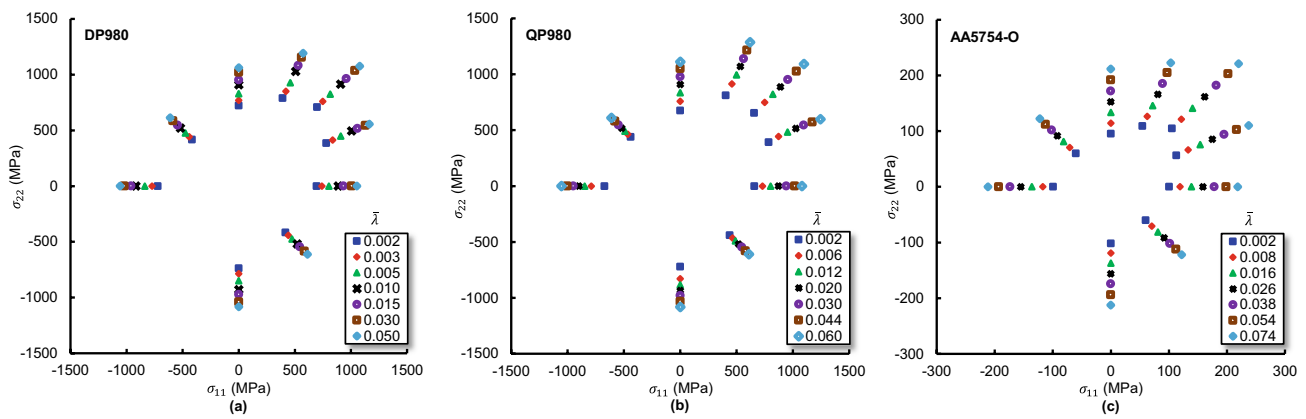


**Fig. 5** Experimental yield loci with the increasing plastic compliance factor of **a** DP980, **b** QP980 and **c** AA5754-O

**Table 1** Yield stresses in MPa and  $r$ -values under uniaxial tension, uniaxial compression, and equi-biaxial tension at the initial yielding ( $\bar{\lambda} = 0.002$ ) of DP980, QP980 and AA5754-O, and data in bold are used to calibrate the parameters in the proposed constitutive model

Yield stress (MPa)	DP980	QP980	AA5754-O
$\sigma_{T0}$	<b>693.8</b>	<b>659.1</b>	<b>100.4</b>
$\sigma_{T15}$	711.2	675.3	94.7
$\sigma_{T30}$	695.1	683.7	95.1
$\sigma_{T45}$	<b>715.0</b>	<b>685.9</b>	<b>95.2</b>
$\sigma_{T60}$	692.5	693.2	95.2
$\sigma_{T75}$	705.9	684.8	91.6
$\sigma_{T90}$	<b>721.7</b>	<b>676.8</b>	<b>95.4</b>
$\sigma_{C0}$	<b>722.2</b>	<b>671.1</b>	<b>99.2</b>
$\sigma_{C45}$	<b>741.3</b>	<b>722.8</b>	<b>94.9</b>
$\sigma_{C90}$	<b>737.4</b>	<b>721.4</b>	<b>101.7</b>
$\sigma_b$	<b>702.6</b>	<b>655.5</b>	<b>105.1</b>
$r$ -value	DP980	QP980	AA5754-O
$r_{T0}$	<b>0.82</b>	<b>0.60</b>	<b>0.65</b>
$r_{T15}$	0.84	0.64	0.61
$r_{T30}$	0.87	0.69	0.62
$r_{T45}$	<b>0.94</b>	<b>0.67</b>	<b>0.65</b>
$r_{T60}$	0.94	0.76	0.67
$r_{T75}$	0.94	0.77	0.70
$r_{T90}$	<b>0.96</b>	<b>0.75</b>	<b>0.72</b>
$r_{C0}$	<b>0.77</b>	<b>0.97</b>	<b>0.60</b>
$r_{C45}$	<b>0.86</b>	<b>0.74</b>	<b>0.75</b>
$r_{C90}$	<b>0.76</b>	<b>0.93</b>	<b>0.62</b>
$r_b$	<b>0.84</b>	<b>0.79</b>	<b>1.29</b>

from the stress vs. strain curves obtained through uniaxial tension, uniaxial compression, biaxial tension, and simple shear based on the principle of plastic work equivalence. As expected, the yield loci expands as  $\bar{\lambda}$  increases. It should be noted that the outermost yield loci in Fig. 5 corresponds to the maximum  $\bar{\lambda}$  that can be achieved using the laser-deposited cruciform specimens.

## 4.2 Non-associated Flow Rule of Sheet Metals

The evolving yield behavior of DP980, QP980, and AA5754-O is observed; however, it is not discussed in detail to maintain brevity. Only the initial yielding ( $\bar{\lambda}=0.002$ ) was selected to show the non-associated characteristic based on

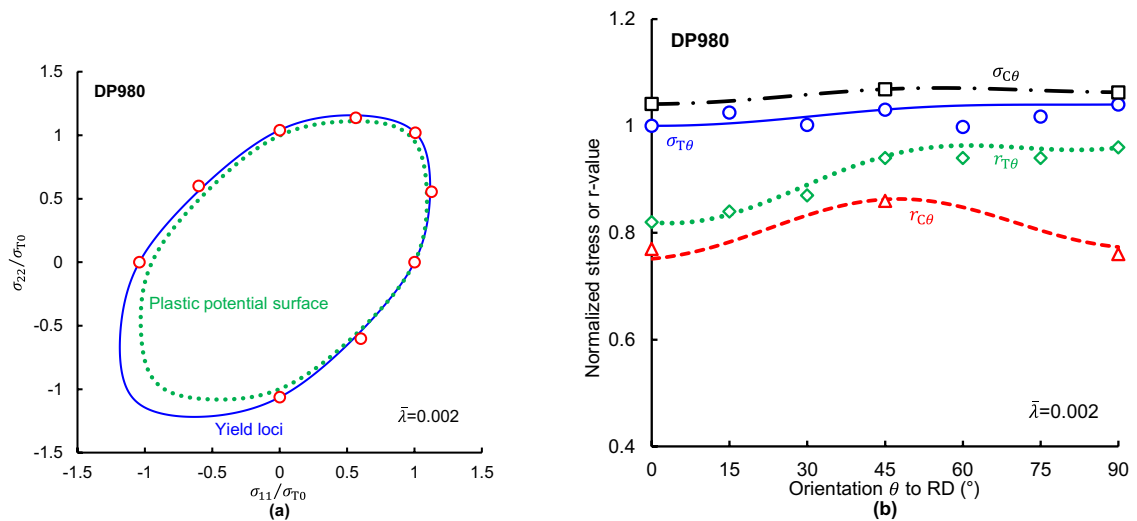


**Fig. 6** **a** Predicted yield loci and plastic potential surface and **b** normalized yield stresses and r-values under uniaxial tension and compression at the initial yielding ( $\bar{\lambda}=0.002$ ) of DP980 (Symbols show the experimental data)

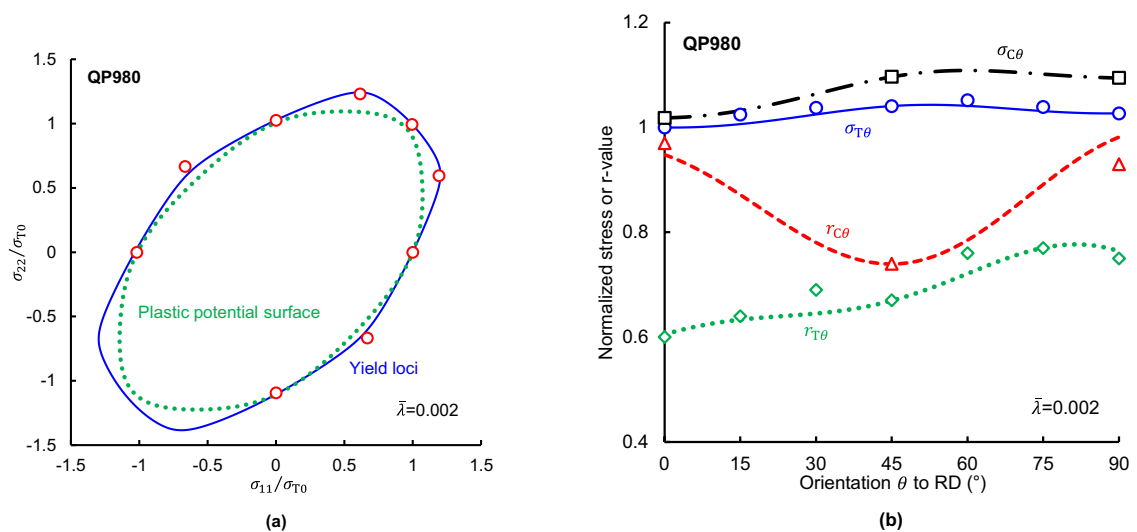


**Fig. 7** **a** Predicted yield loci and plastic potential surface and **b** normalized yield stresses and r-values under uniaxial tension and compression at the initial yielding ( $\bar{\lambda}=0.002$ ) of QP980 (Symbols show the experimental data)

the presented constitutive model in Sect. 3. Table 1 summarizes the yield stresses and r-values under uniaxial tension, uniaxial compression, and equi-biaxial tension at  $\bar{\lambda}=0.002$  of DP980, QP980 and AA5754-O. The numbers in bold in Table 1 are used to identify the model parameters in the yield stress function and plastic potential function. The

determined parameters in the constitutive model are summarized in Table 2.

The convenient capture of SD effect (along  $0^\circ$ ,  $45^\circ$ , and  $90^\circ$  to the RD) is achieved by  $f_{Quad}(\sigma, \bar{\lambda})$  in Eq. (2) with explicit identification of  $a_y$  to  $g_y$  according to Eq. (3).



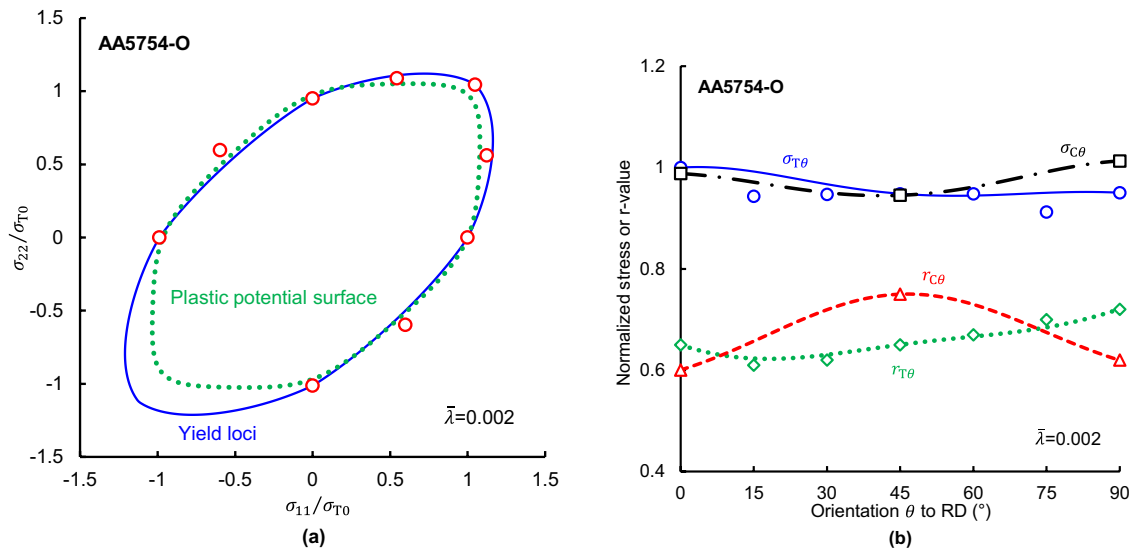


**Fig. 8** **a** Predicted yield loci and plastic potential surface and **b** normalized yield stresses and r-values under uniaxial tension and compression at the initial yielding ( $\bar{\lambda}=0.002$ ) of AA5754-O (Symbols show the experimental data)

Furthermore, the combination of two independent exponents  $n_{HH}$  and  $n_{IHH}$  provides high flexibility in describing the shape of the yield surface. Note that the Particle Swarm Optimization function in MATLAB is adopted to determine the values of  $a_p$  to  $h_p$  in the plastic potential function, and the exponent  $k_p$  is set to 6 for DP980 and QP980, and 8 for AA5754-O, respectively.

The yield loci and plastic potential in the normal plane at the initial yielding ( $\bar{\lambda}=0.002$ ) of DP980, QP980, and AA5754-O are presented in Figs. 6(a), 7(a), 8(a), with the experimental data represented by hollow red spots. The normalized yield stresses and r-values under uniaxial loading, obtained from experiments and predicted by the constitutive model, are compared in Figs. 6(b), 7(b), 8(b). On the one hand, the comparison of the results demonstrates the good agreement between the presented constitutive model and experimental data for each material. Note that the yield surface of QP980 at the initial yielding is obviously beyond the quadratic Mises yield surface, as shown in Fig. 7(a), which can be accurately captured by

the developed yield criterion attributed to two independent exponents. On the other hand, the clear difference between the yield surface and plastic potential, especially in the compression region of the normal plane, of DP980, QP980, and AA5754-O highlights the non-associated characteristic in the flow rule.

Furthermore, the results presented in Figs. 6(b), 7(b), 8(b) indicate that yield stresses including both  $\sigma_{T\theta}$  and  $\sigma_{C\theta}$  are isotropic. However, all investigated materials exhibited a pronounced orientation dependence or planar anisotropy in  $r_{T\theta}$ -value and  $r_{C\theta}$ -value. Much more complex functions and parameter identification procedures are required to accurately capture the yield behavior in Figs. 6–8 by an AFR model. An in-depth understanding of the non-AFR feature in yielding sheet metals is critical for fully exploiting materials and multi-scale modeling of sheet metals, and the insight into their micro-scaled mechanisms will be studied through microscopic observations and crystal plasticity simulations.

### 4.3 Non-quadratic Characteristics of Yield Surface and Plastic Potential

The yield stresses and plastic strain ratios under the plane strain state play a significant role in the validation of material models. Table 3 lists the yield stresses and ratios of plastic strain under plane strain (PS0 and PS90) obtained from laser-deposited cruciform biaxial tensile testing, as well as the yield stresses under simple shear obtained from in-plane torsion testing at the initial yielding ( $\bar{\lambda}=0.002$ ) of DP980, QP980, and AA5754-O. In order to investigate the non-quadratic characteristic of yield surface, the quadratic yield criterion  $f_{\text{Quad}}(\sigma, \bar{\lambda})$  in Eq. (2) is employed to predict the yield loci of DP980, QP980, and AA5754-O at the initial yielding ( $\bar{\lambda}=0.002$ ). The calculated yield loci are then compared with that calculated using the coupled yield criterion  $f_{\text{Coup}}(\sigma, \bar{\lambda})$  in Fig. 9. Note that the exponent  $m$  is set to 3 in this work, while  $n_{\text{HH}}$  and  $n_{\text{HH}}$  in Table 2 are determined following the proposed approach from reference [34]. As shown in Fig. 9,  $f_{\text{Quad}}(\sigma, \bar{\lambda})$  maintains the accurate prediction of uniaxial tensile and compressive yield stresses, as well as the equibiaxial stress ( $\sigma_b$ ), in agreement with the non-quadratic  $f_{\text{Coup}}(\sigma, \bar{\lambda})$ . However,  $f_{\text{Quad}}(\sigma, \bar{\lambda})$  in Eq. (2) over-estimates the yield stresses under plane strain for DP980 and AA5754-O, while underestimating the yield stresses under plane strain for QP980 at the initial yielding ( $\bar{\lambda}=0.002$ ).

To quantitatively evaluate the accuracy of predicting experimental yield loci using both quadratic and non-quadratic functions, a mean square root (MSR) error is calculated by the following metric:

$$\Delta_{\text{YL}}(\bar{\lambda}) = \sqrt{\frac{1}{N} \sum_i^N w_i \cdot (\delta_{\text{YL}}(i))^2} \tag{6}$$

where

$$\delta_{\text{YL}}(i) = \frac{\sqrt{(\sigma_{11,\text{Cal.}}(i) - \sigma_{11,\text{Exp.}}(i))^2 + (\sigma_{22,\text{Cal.}}(i) - \sigma_{22,\text{Exp.}}(i))^2 + (\sigma_{12,\text{Cal.}}(i) - \sigma_{12,\text{Exp.}}(i))^2}}{\sqrt{(\sigma_{11,\text{Exp.}}(i))^2 + (\sigma_{22,\text{Exp.}}(i))^2 + (\sigma_{12,\text{Exp.}}(i))^2}} \tag{7}$$

where  $N$  is the number of experimental data sets, which consist of uniaxial tension with 7 various angles to RD, uniaxial compression with 3 various angles to RD, equibiaxial tension, plane strain along RD, plane strain along TD (with 90° to the RD) and simple shear in this work. The weighting

factor  $w_i=2.0$  associated with 15°, 30°, 45°, 60°, and 75° reflects the inclusion of contributions at angles of 105°, 120°, 135°, 150°, and 165°, respectively, while other experimental data sets possess a weighting factor  $w_i=1.0$ . The ratio  $\delta_{\text{YL}}(i)$  represents the "distance" between the experimental and calculated data points normalized by the "distance" between the experimental data point and the origin in the  $\sigma_{11}$ - $\sigma_{22}$ - $\sigma_{12}$  space. Figure 10(a) presents the variation of MSR errors  $\Delta_{\text{YL}}(\bar{\lambda})$ , with increasing plastic compliance factor  $\bar{\lambda}$ . For DP980, both  $f_{\text{Quad}}(\sigma, \bar{\lambda})$  and  $f_{\text{Coup}}(\sigma, \bar{\lambda})$  give the  $\Delta_{\text{YL}}(\bar{\lambda})$  less than 2.0% during the plastic deformation with increasing  $\bar{\lambda}$  from 0.002 to 0.050. For QP980, the  $\Delta_{\text{YL}}(\bar{\lambda})$  predicted by  $f_{\text{Quad}}(\sigma, \bar{\lambda})$  decreases rapidly to less than 2.0% when  $\bar{\lambda}$  increases from 0.002 to 0.004, and then goes close to that predicted by  $f_{\text{Coup}}(\sigma, \bar{\lambda})$ . For AA5754-O, the  $\Delta_{\text{YL}}(\bar{\lambda})$  predicted by  $f_{\text{Quad}}(\sigma, \bar{\lambda})$  varies around 3.0%, which is much higher than that predicted by  $f_{\text{Coup}}(\sigma, \bar{\lambda})$ . Further, the average errors throughout loading histories, as expressed by Eq. (8), are calculated and presented for comparison in Fig. 10(b).

$$\bar{\Delta}_{\text{YL}} = \frac{1}{\bar{\lambda}_L} \int_0^{\bar{\lambda}_L} \Delta_{\text{YL}}(\bar{\lambda}) d\bar{\lambda} \tag{8}$$

where  $\bar{\lambda}_L$  means the largest  $\bar{\lambda}$  achieved using the laser-deposited cruciform specimens, as shown in Fig. 5. It should be noted that the average errors  $\bar{\Delta}_{\text{YL}}$  of QP980 calculated from both  $f_{\text{Quad}}(\sigma, \bar{\lambda})$  and  $f_{\text{Coup}}(\sigma, \bar{\lambda})$  are below 1.0%, which is related to nearly quadratic yield surface exhibited by QP980 at higher plastic strain levels when  $\bar{\lambda}>0.028$ . The error in predicting the yield behavior of DP980 can be decreased from 1.4% to 0.7% when employing the non-quadratic functions rather than quadratic functions. It is vital to consider

the non-quadratic characteristic of AA5754-O when establishing the yield criterion.

The average errors in angle, denoted as  $\bar{\Delta}_\beta$ , were calculated to evaluate the accuracy of predicting plastic strain directions under plane strain and equibiaxial tension using

**Table 2** Parameters in the developed yield stress function ( $f_{\text{Coup}}(\sigma, \bar{\lambda})$ ) and plastic potential function ( $\bar{\sigma}_p(\sigma, \bar{\lambda})$ ) of DP980, QP980 and AA5754-O at the initial yielding ( $\bar{\lambda}=0.002$ )

Parameter in $f_{\text{Coup}}(\sigma, \bar{\lambda})$	DP980	QP980	AA5754-O
$a_y(\text{MPa}^{-3})$	1.6966E-10	0.9257E-10	-0.1874E-7
$b_y(\text{MPa}^{-3})$	0.8352E-10	2.8057E-10	0.9973E-7
$c_y(\text{MPa}^{-3})$	0.2746E-10	0.7739E-10	-0.9089E-7
$d_y(\text{MPa}^{-6})$	0.7980E-17	1.1564E-17	0.1012E-11
$e_y(\text{MPa}^{-6})$	0.6642E-17	0.8671E-17	0.1105E-11
$f_y(\text{MPa}^{-6})$	0.7703E-17	1.0136E-17	0.1507E-11
$g_y(\text{MPa}^{-6})$	2.0017E-17	2.2926E-17	0.4808E-11
$m$	3	3	3
$n_{\text{HH}}$	6.4	2.7	1.4
$n_{\text{IHH}}$	2.7	40	2.7
Parameter in $\bar{\sigma}_p(\sigma, \bar{\lambda})$	DP980	QP980	AA5754-O
$a_p$	-0.0269	0.0052	-0.0176
$b_p$	0.0008	0.0523	-0.0028
$c_p$	-0.0297	0.0994	-0.1098
$d_p$	0.6272	0.5142	0.7481
$e_p$	0.5456	0.4553	0.4014
$f_p$	0.9872	0.986	0.9643
$g_p$	0.9602	0.9431	1.0349
$h_p$	-0.5013	0.4701	0.5172
$k_p$	6	6	8

**Table 3** Yield stresses and plastic strain ratios under plane strain (PS0 and PS90) obtained from laser-deposited cruciform biaxial tensile testing and yield stresses under simple shear obtained from in-plane torsion testing at the initial yielding ( $\bar{\lambda}=0.002$ ) of DP980, QP980 and AA5754-O

Yield stress (MPa)	DP980	QP980	AA5754-O
$\sigma_{\text{PS0}_R}$	781.0	784.6	112.9
$\sigma_{\text{PS0}_T}$	385.8	392.5	56.4
$\sigma_{\text{PS90}_R}$	391.4	404.6	54.6
$\sigma_{\text{PS90}_T}$	789.9	811.1	109.4
$\sigma_{\text{SS}}$	417.1	439.4	60.0
Plastic strain ratios	DP980	QP980	AA5754-O
$\sigma_{\text{PS0}_R}/\sigma_{\text{PS0}_T}$	2.02	2.00	2.00
$r_{\text{PS0}} = \Delta\varepsilon_2^p/\Delta\varepsilon_1^p$	-0.0262	-0.043	-0.0286
$\sigma_{\text{PS0}_R}/\sigma_{\text{PS0}_T}$	2.02	2.00	2.00
$r_{\text{PS0}} = \Delta\varepsilon_2^p/\Delta\varepsilon_1^p$	-0.0135	-0.033	-0.0266

the plastic potential function. The metric is defined as follows:

$$\bar{\Delta}_\beta = \frac{1}{3} \sum \left| \tan^{-1}(r_{\theta, \text{Cal.}}) - \tan^{-1}(r_{\theta, \text{Exp.}}) \right| \quad (9)$$

where  $\theta$  represents the plastic strain ratios under the plane strain along  $0^\circ$  and  $90^\circ$  to the rolling direction (RD) and the r-value under equi-biaxial tension. Specifically,  $\theta$  takes the values "PS0", "PS90", and "b" for the respective plastic strain ratios.

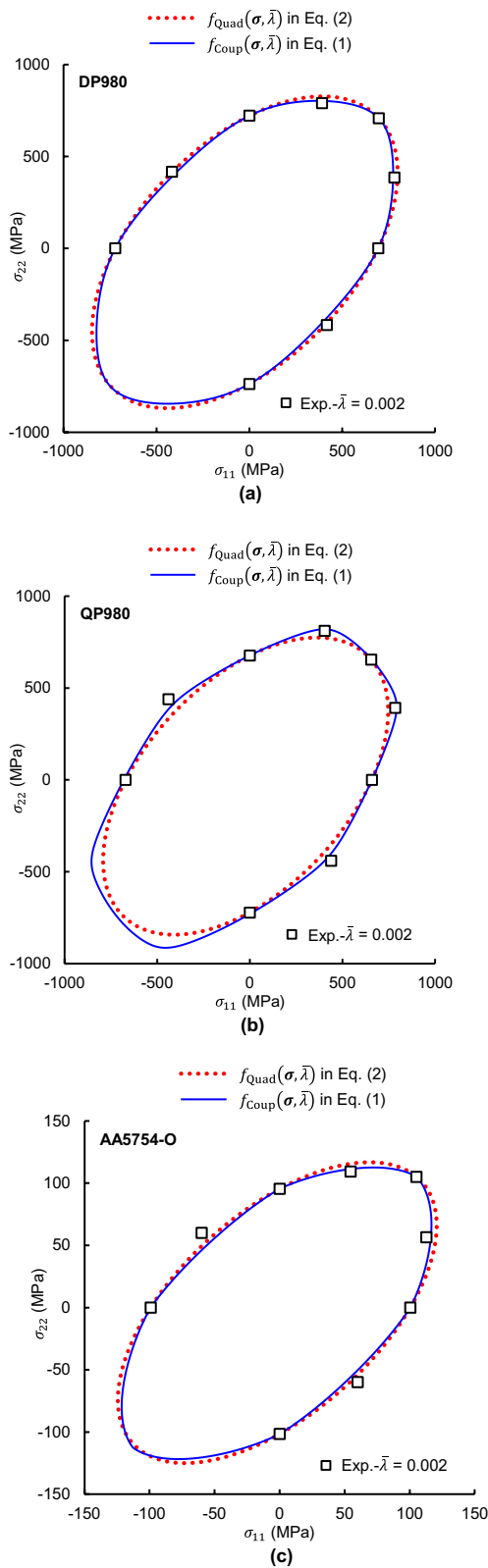


**Fig. 9** Comparison of yield loci measured from experiments and calculated from the quadratic function  $f_{Quad}(\sigma, \bar{\lambda})$  in Eq. (2) and the coupled model  $f_{Coup}(\sigma, \bar{\lambda})$  in Eq. (1) at the initial yielding ( $\bar{\lambda}=0.002$ ) of (a) DP98, (b) QP980 and (c) AA5754-O

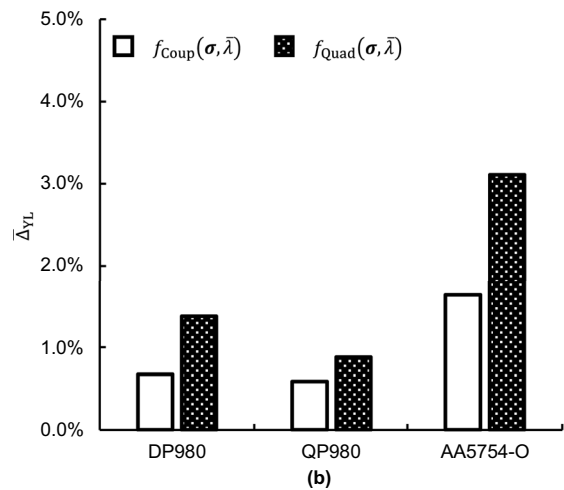
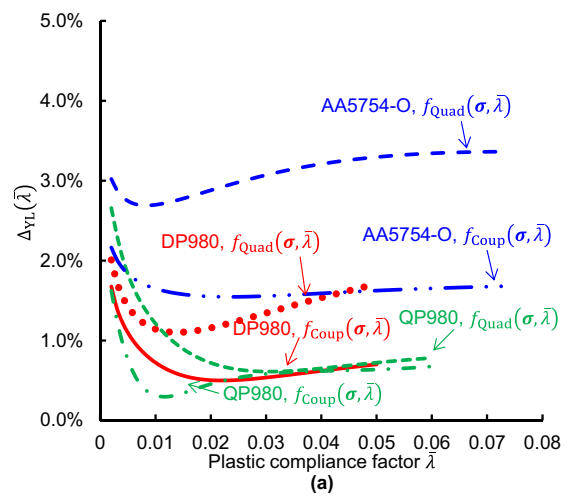


**Fig. 10** **a** Variation of MSR errors  $\Delta_{YL}(\bar{\lambda})$  with the increasing plastic compliance factor  $\bar{\lambda}$  and **b** average MSR errors  $\bar{\Delta}_{YL}$  in predictions of yield loci calculated from the quadratic yield function  $f_{Quad}(\sigma, \bar{\lambda})$  and the coupled yield function  $f_{Coup}(\sigma, \bar{\lambda})$  of DP980, QP980 and AA5754-O

Figure 11 illustrates the comparison of  $\bar{\Delta}_\beta$  values for DP980, QP980, and AA5754-O when using the quadratic ( $k_p=2$  in Eq. (5)) and non-quadratic ( $k_p=6$  for DP980 and QP980 while  $k_p=8$  for AA5754-O) plastic potential functions to calculate the plastic strain ratios. For DP980, the errors decreased from  $3.1^\circ$  to  $0.9^\circ$ ; for QP980, from  $6.1^\circ$  to  $3.9^\circ$ ; and for the investigated aluminium alloy AA5754-O, from  $7.0^\circ$  to  $0.2^\circ$ . The comparison demonstrates that the use of a non-quadratic function rather than a quadratic function decreases the errors in predicting plastic strain directions for the investigated materials, especially for AA5754-O.

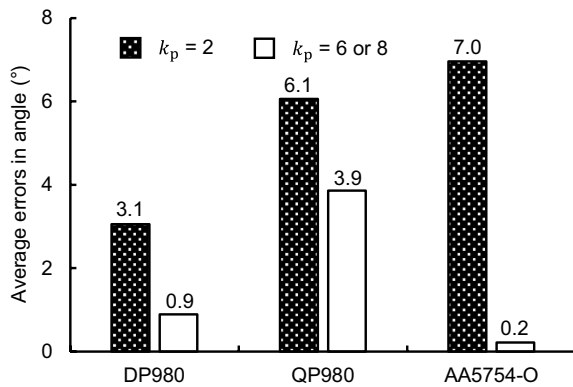


**Fig. 11** Average errors in angle when predicting plastic strain directions under plane strain and equi-biaxial tension by quadratic ( $k_p=2$  in Eq. (5)) and non-quadratic ( $k_p=6$  for DP980 and QP980 while  $k_p=8$  for AA5754-O in Eq. (5)) plastic potential function

## 5 Conclusions

A comprehensive investigation is conducted to examine the non-associated and non-quadratic characteristics of yielding in lightweight sheet metals, specifically dual-phase steel DP980, TRIP-assisted steel QP980, and aluminum alloy AA5754-O. The main conclusions are as follows:

- (1) The presented plasticity model under non-AFR shows good agreement with experimental data, including yield loci, yield stresses, and  $r$ -values under various loading conditions.
- (2) Clear differences are observed between the yield surface and plastic potential. The mechanical responses exhibited planar isotropy with respect to stress levels but displays planar anisotropy with respect to  $r$ -values.
- (3) Consideration of the non-quadratic characteristic of AA5754-O when selecting the yield stress function is found to be significant and necessary. However, the incorporation of non-quadratic functions only resulted in a slight reduction in the errors when predicting yield loci for advanced high-strength steels.
- (4) By incorporating non-quadratic plastic potential functions, the average errors in angle when predicting plastic strain directions are significantly reduced. For DP980, the errors decreased from  $3.1^\circ$  to  $0.9^\circ$ ; for QP980, from  $6.1^\circ$  to  $3.9^\circ$ ; and for AA5754-O, from  $7.0^\circ$  to  $0.2^\circ$ . This highlights the importance of considering the non-quadratic characteristic in the plastic potential for accurate modeling of aluminum alloys.

**Acknowledgements** YH acknowledges the support of the BK21 Four program (SNU Materials Education/Research Division for Creative Global Leaders). JM appreciates the financial support

from the Science and Technology Commission of Shanghai Municipality (grant number: 21170711200). MGL appreciates the grant from NRF (No. 2022R1A2C2009315) and Institute of Engineering Research at SNU. Also, this work was partially supported by the KEIT (1415185590, 20022438) funded by the Ministry of Trade, Industry & Energy (MOTIE, Korea).

## Declarations

**Conflict of interest** On behalf of all the authors, the corresponding author states that there is no conflict of interest.

**Open Access** This article is licensed under a Creative Commons Attribution 4.0 International License, which permits use, sharing, adaptation, distribution and reproduction in any medium or format, as long as you give appropriate credit to the original author(s) and the source, provide a link to the Creative Commons licence, and indicate if changes were made. The images or other third party material in this article are included in the article's Creative Commons licence, unless indicated otherwise in a credit line to the material. If material is not included in the article's Creative Commons licence and your intended use is not permitted by statutory regulation or exceeds the permitted use, you will need to obtain permission directly from the copyright holder. To view a copy of this licence, visit <http://creativecommons.org/licenses/by/4.0/>.

## References

1. Hill, R.: A theory of the yielding and plastic flow of anisotropic metals. *Proc. R. Soc. Lond. Ser. A Math. Phys. Sci.* **193**, 281–297 (1948). <https://doi.org/10.1098/rspa.1948.0045>
2. Barlat, F., Lian, J.: Plastic behavior and stretchability of sheet metals I. A yield function for orthotropic sheets under plane-stress conditions. *Int. J. Plast.* **5**, 51–66 (1989). [https://doi.org/10.1016/0749-6419\(89\)90019-3](https://doi.org/10.1016/0749-6419(89)90019-3)
3. Hosford, W.: A generalized isotropic yield criterion. *J. Appl. Mech.* **39**, 607–609 (1972). <https://doi.org/10.1115/1.3422732>
4. Gotoh, M.: A theory of plastic anisotropy based on a yield function of fourth order (plane stress state)—I. *Int. J. Mech. Sci.* **19**, 505–512 (1977). [https://doi.org/10.1016/0020-7403\(77\)90044-3](https://doi.org/10.1016/0020-7403(77)90044-3)
5. Tong, W.: A plane stress anisotropic plastic flow theory for orthotropic sheet metals. *Int. J. Plast.* **22**, 497–535 (2006). <https://doi.org/10.1016/j.ijplas.2005.04.005>
6. Soare, S., Yoon, J.W., Cazacu, O.: On the use of homogeneous polynomials to develop anisotropic yield functions with applications to sheet forming. *Int. J. Plast.* **24**, 915–944 (2008). <https://doi.org/10.1016/j.ijplas.2007.07.016>
7. Hu, W.: A novel quadratic yield model to describe the feature of multi-yield-surface of rolled sheet metals. *Int. J. Plast.* **23**, 2004–2028 (2007). <https://doi.org/10.1016/j.ijplas.2007.01.016>
8. Barlat, F., Brem, J.C., Yoon, J.W., Chung, K., Dick, R.E., Lege, D.J., Pourghrat, F., Choi, S.H., Chu, E.: Plane stress yield function for aluminum alloy sheets - part 1: theory. *Int. J. Plast.* **19**, 1297–1319 (2003). [https://doi.org/10.1016/S0749-6419\(02\)00019-0](https://doi.org/10.1016/S0749-6419(02)00019-0)
9. Banabic, D., Aretz, H., Comsa, D., Paraianu, L.: An improved analytical description of orthotropy in metallic sheets. *Int. J. Plast.* **21**, 493–512 (2005). <https://doi.org/10.1016/j.ijplas.2004.04.003>
10. Barlat, F., Aretz, H., Yoon, J.W., Karabin, M.E., Brem, J.C., Dick, R.E.: Linear transformation-based anisotropic yield functions. *Int. J. Plast.* **21**, 1009–1039 (2005). <https://doi.org/10.1016/j.ijplas.2004.06.004>

11. Bron, F., Besson, J.: A yield function for anisotropic materials application to aluminum alloys. *Int. J. Plast.* **20**, 937–963 (2004). <https://doi.org/10.1016/j.ijplas.2003.06.001>
12. Cazacu, O., Barlat, F.: Generalization of Drucker's yield criterion to orthotropy. *Math. Mech. Solids* **6**, 613–630 (2001). <https://doi.org/10.1177/108128650100600603>
13. Soare, S., Barlat, F.: Convex polynomial yield functions. *J. Mech. Phys. Solids* **58**, 1804–1818 (2010). <https://doi.org/10.1016/j.jmps.2010.08.005>
14. Aretz, H., Barlat, F.: New convex yield functions for orthotropic metal plasticity. *Int. J. Non Linear Mech.* **51**, 97–111 (2013). <https://doi.org/10.1016/j.ijnonlinmec.2012.12.007>
15. Cazacu, O.: New yield criteria for isotropic and textured metallic materials. *Int. J. Solids Struct.* **139**, 200–210 (2018). <https://doi.org/10.1016/j.ijsolstr.2018.01.036>
16. Yoshida, F., Hamasaki, H., Uemori, T.: A user-friendly 3D yield function to describe anisotropy of steel sheets. *Int. J. Plast.* **45**, 119–139 (2013). <https://doi.org/10.1016/j.ijplas.2013.01.010>
17. Spitzig, W.A., Richmond, O.: The effect of pressure on the flow stress of metals. *Acta Metall.* **32**, 457–463 (1984). [https://doi.org/10.1016/0001-6160\(84\)90119-6](https://doi.org/10.1016/0001-6160(84)90119-6)
18. Stoughton, T.B.: A non-associated flow rule for sheet metal forming. *Int. J. Plast.* **18**, 687–714 (2002). [https://doi.org/10.1016/S0749-6419\(01\)00053-5](https://doi.org/10.1016/S0749-6419(01)00053-5)
19. Hou, Y., Myung, D., Park, J.K., Min, J., Lee, H.R., El-Aty, A.A., Lee, M.G.: A review of characterization and modelling approaches for sheet metal forming of lightweight metallic materials. *Materials* **16**, 836 (2023). <https://doi.org/10.3390/ma16020836>
20. Stoughton, T.B., Yoon, J.W.: A pressure-sensitive yield criterion under a non-associated flow rule for sheet metal forming. *Int. J. Plast.* **20**, 705–731 (2004). [https://doi.org/10.1016/S0749-6419\(03\)00079-2](https://doi.org/10.1016/S0749-6419(03)00079-2)
21. Min, J., Carsley, J.E., Lin, J., Wen, Y., Kuhlenkotter, B.: A non-quadratic constitutive model under non-associated flow rule of sheet metals with anisotropic hardening: modeling and experimental validation. *Int. J. Mech. Sci.* **119**, 343–359 (2016). <https://doi.org/10.1016/j.ijmecsci.2016.10.027>
22. Lee, E.H., Stoughton, T.B., Yoon, J.W.: A yield criterion through coupling of quadratic and non-quadratic functions for anisotropic hardening with non-associated flow rule. *Int. J. Plast.* **99**, 120–143 (2017). <https://doi.org/10.1016/j.ijplas.2017.08.007>
23. Park, N., Stoughton, T.B., Yoon, J.W.: A criterion for general description of anisotropic hardening considering strength differential effect with non-associated flow rule. *Int. J. Plast.* **121**, 76–100 (2019). <https://doi.org/10.1016/j.ijplas.2019.04.015>
24. Hu, Q., Yoon, J.W.: Analytical description of an asymmetric yield function (Yoon 2014) by considering anisotropic hardening under non-associated flow rule. *Int. J. Plast.* **140**, 102978 (2021). <https://doi.org/10.1016/j.ijplas.2021.102978>
25. Hou, Y., Du, K., Abd El-Aty, A., Lee, M.G., Min, J.: Plastic anisotropy of sheet metals under plane strain loading: a novel non-associated constitutive model based on fourth-order polynomial functions. *Mater. Des.* **223**, 111187 (2022). <https://doi.org/10.1016/j.matdes.2022.111187>
26. Lou, Y., Zhang, C., Zhang, S., Yoon, J.W.: A general yield function with differential and anisotropic hardening for strength modelling under various stress states with non-associated flow rule. *Int. J. Plast.* **158**, 103414 (2022). <https://doi.org/10.1016/j.ijplas.2022.103414>
27. Hou, Y., Min, J., Guo, N., Shen, Y., Lin, J.: Evolving asymmetric yield surfaces of quenching and partitioning steels: characterization and modeling. *J. Mater. Process. Technol.* **290**, 116979 (2021). <https://doi.org/10.1016/j.jmatprotec.2020.116979>
28. Lou, Y., Yoon, J.W.: Anisotropic yield function based on stress invariants for BCC and FCC metals and its extension to ductile fracture criterion. *Int. J. Plast.* **101**, 125–155 (2018). <https://doi.org/10.1016/j.ijplas.2017.10.012>
29. Chen, Z., Wang, Y., Lou, Y.: User-friendly anisotropic hardening function with non-associated flow rule under the proportional loadings for BCC and FCC metals. *Mech. Mater.* **165**, 104190 (2022). <https://doi.org/10.1016/j.mechmat.2021.104190>
30. Hou, Y., Min, J., Lin, J., Lee, M.G.: Modeling stress anisotropy, strength differential, and anisotropic hardening by coupling quadratic and stress-invariant-based yield functions under non-associated flow rule. *Mech. Mater.* **174**, 104458 (2022). <https://doi.org/10.1016/j.mechmat.2022.104458>
31. Hu, Q., Chen, J., Yoon, J.W.: A new asymmetric yield criterion based on Yld 2000–2d under both associated and non-associated flow rules: modeling and validation. *Mech. Mater.* **167**, 104245 (2022). <https://doi.org/10.1016/j.mechmat.2022.104245>
32. Safaei, M., Lee, M.G., De Waele, W.: Evaluation of stress integration algorithms for elastic-plastic constitutive models based on associated and non-associated flow rules. *Comput. Methods Appl. Mech. Eng.* **295**, 414–445 (2015). <https://doi.org/10.1016/j.cma.2015.07.014>
33. Du, K., Huang, S., Hou, Y., Wang, H., Wang, Y., Zheng, W., Yuan, X.: Characterization of the asymmetric evolving yield and flow of 6016–T4 aluminum alloy and DP490 steel. *J. Mater. Sci. Technol.* **133**, 209–229 (2023). <https://doi.org/10.1016/j.jmst.2022.05.040>
34. Hou, Y., Min, J., Stoughton, T.B., Lin, J., Carsley, J.E., Carlson, B.E.: A non-quadratic pressure-sensitive constitutive model under non-associated flow rule with anisotropic hardening: modeling and validation. *Int. J. Plast.* **135**, 102808 (2020). <https://doi.org/10.1016/j.ijplas.2020.102808>
35. Mu, Z., Zhao, J., Meng, Q., Sun, H., Yu, G.: Anisotropic hardening and evolution of r-values for sheet metal based on evolving non-associated Hill48 model. *Thin Walled Struct.* **171**, 108791 (2022). <https://doi.org/10.1016/j.tws.2021.108791>
36. Bandyopadhyay, K., Basak, S., Panda, S.K., Saha, P., Zhou, N.: Application of non-associated flow rule for prediction of nonuniform material flow during deep drawing of tailor welded blanks. *Proc. Inst. Mech. Eng. Part B J. Eng. Manuf.* (2022). <https://doi.org/10.1177/09544054221110958>
37. Lee, E.H., Stoughton, T.B., Yoon, J.W.: Kinematic hardening model considering directional hardening response. *Int. J. Plast.* **110**, 145–165 (2018). <https://doi.org/10.1016/j.ijplas.2018.06.013>
38. Lee, E.H., Choi, H., Stoughton, T.B., Yoon, J.W.: Combined anisotropic and distortion hardening to describe directional response with Bauschinger effect. *Int. J. Plast.* **122**, 73–88 (2019). <https://doi.org/10.1016/j.ijplas.2019.07.007>
39. Barlat, F., Gracio, J.J., Lee, M.G., Rauch, E.F., Vincze, G.: An alternative to kinematic hardening in classical plasticity. *Int. J. Plast.* **27**, 1309–1327 (2011). <https://doi.org/10.1016/j.ijplas.2011.03.003>
40. Hou, Y., Lee, M.G., Lin, J., Min, J.: Experimental characterization and modeling of complex anisotropic hardening in quenching and partitioning (Q&P) steel subject to biaxial non-proportional loadings. *Int. J. Plast.* **156**, 103347 (2022). <https://doi.org/10.1016/j.ijplas.2022.103347>
41. Hu, Q., Yoon, J.W.: Anisotropic distortional hardening based on deviatoric stress invariants under non-associated flow rule. *Int. J. Plast.* **151**, 103214 (2022). <https://doi.org/10.1016/j.ijplas.2022.103214>
42. Shen, F., Münstermann, S., Lian, J.: Forming limit prediction by the Marciniak-Kuczynski model coupled with the evolving non-associated Hill48 plasticity model. *J. Mater. Process. Technol.* **287**, 116384 (2021). <https://doi.org/10.1016/j.jmatprotec.2019.116384>
43. Vobejda, R., Šebek, F., Kubík, P., Petruška, J.: Solution to problems caused by associated non-quadratic yield functions with

respect to the ductile fracture. *Int. J. Plast.* **154**, 103301 (2022). <https://doi.org/10.1016/j.ijplas.2022.103301>

44. Wu, H., Zhuang, X., Zhang, W., Zhao, Z.: Anisotropic ductile fracture: experiments, modeling, and numerical simulations. *J. Mater. Res. Technol.* (2022). <https://doi.org/10.1016/j.jmrt.2022.07.128>
45. Hou, Y., Zhang, X., Min, J., Lee, M.G.: Plastic deformation of ultra-thin pure titanium sheet subject to tension-compression loadings. *IOP Conf. Ser. Mater. Sci. Eng.* **1270**, 012020 (2022). <https://doi.org/10.1088/1757-899X/1270/1/012020>
46. Tekkaya, A., Pöhlandt, K., Lange, K.: Determining stress-strain curves of sheet metal in the plane torsion test. *CIRP Ann.* **31**, 171–174 (1982). [https://doi.org/10.1016/S0007-8506\(07\)63291-0](https://doi.org/10.1016/S0007-8506(07)63291-0)
47. ISO: ISO16842, Metallic materials-sheet and strip-biaxial tensile testing method using a cruciform test piece (2014)
48. Hou, Y., Min, J., Lin, J., Carsley, J.E., Stoughton, T.B.: Cruciform specimen design for large plastic strain during biaxial tensile testing. *J. Phys. Conf. Ser.* **1063**, 012160 (2018)
49. Hou, Y., Min, J., Lin, J., Carsley, J.E., Stoughton, T.B.: Plastic instabilities in AA5754-O under various stress states. *IOP Conf. Ser. Mater. Sci. Eng.* **418**, 012050 (2018)
50. Jones, E.M.C., Iadicola, M.A.: A good practices guide for digital image correlation. *Int. Dig. Image Correl. Soc.* **10**, 308–312 (2018)
51. Hou, Y., Min, J., Guo, N., Lin, J., Carsley, J.E., Stoughton, T.B., Traphöner, H., Clausmeyer, T., Tekkaya, A.E.: Investigation of evolving yield surfaces of dual-phase steels. *J. Mater. Process. Technol.* **287**, 116314 (2021). <https://doi.org/10.1016/j.jmatp.rotec.2019.116314>



**Yong Hou** received his Ph.D. degree from Tongji University (Shanghai, China) in 2021. He is currently a BK21 postdoctoral researcher at the Department of Materials Science and Engineering & RIAM at Seoul National University (Seoul, Korea). His research interests include plasticity modeling, mechanical characterization, advanced lightweight materials, multi-scale modeling, and sheet metal forming.



**Junying Min** is professor/vice dean of the School of Mechanical Engineering, Tongji University. He is the deputy director of CDZM. His research interests include advanced forming processes, mechanical characterization and constitutive modeling, and hybrid components and processes of lightweight materials. He was a postdoc at the University of Hawaii and University of Michigan from 2013 to 2014. He conducted research at the Ruhr-University Bochum from 2015 to 2017 as an Alexander von

Humboldt fellow. He is member of expert committee of China Auto Lightweight Technology Innovation Strategy Alliance. To date he has published more than 140 peer-reviewed papers with over 40 in the JCR Q1 journals with international reputation and 3 monographs with his co-authors and has over 20 invention patents filed/granted.



**Myoung-Gyu Lee** is currently a Full Professor at the Department of Materials Science and Engineering at Seoul National University, Korea. He received his Ph.D. from SNU in 2004. His main research interests include multiscale and multiphysics modeling and simulations of structural materials for optimizing manufacturing processes, plasticity theory, and constitutive model development for highly non-linear and anisotropic metals.